Saynisch, J., Petereit, J., Irrgang, C., Kuvshinov, A., Thomas, M. (2016): Impact of climate variability on the tidal oceanic magnetic signal - a model based sensitivity study. - *Journal of Geophysical Research*, *121*, 8, pp. 5931—5941.

DOI: http://doi.org/10.1002/2016JC012027

AGU PUBLICATIONS

JGR

Journal of Geophysical Research: Oceans

RESEARCH ARTICLE
10.1002/2016JC012027

Key Points:
- Climate variability impacts ocean electric conductivity distribution
- Climate variability can significantly influence oceanic tidal magnetic signals
- Climate induced ocean variability is in principle separable in magnetic observations

Correspondence to:
J. Saynisch,
saynisch@gfz-potsdam.de

Citation:
Saynisch, J., J. Petereit, C. Irrgang, A. Kuvshinov, and M. Thomas (2016), Impact of climate variability on the tidal oceanic magnetic signal—A model-based sensitivity study, *J. Geophys. Res. Oceans*, *121*, 5931–5941, doi:10.1002/2016JC012027.

Received 3 JUN 2016
Accepted 14 JUL 2016
Accepted article online 18 JUL 2016
Published online 16 AUG 2016

Impact of climate variability on the tidal oceanic magnetic signal—A model-based sensitivity study

J. Saynisch[1], J. Petereit[1], C. Irrgang[1,2], A. Kuvshinov[3], and M. Thomas[1,2]

[1]Earth System Modelling, Helmholtz Centre Potsdam, GFZ German Research Centre, Potsdam, Germany, [2]Institute of Meteorology, Freie Universität-Berlin, Berlin, Germany, [3]Institute of Geophysics, ETHZurich, Zurich, Switzerland

Abstract ESA's satellite magnetometer mission Swarm is supposed to lower the limit of observability for oceanic processes. While periodic magnetic signals from ocean tides are already detectable in satellite magnetometer observations, changes in the general ocean circulation are yet too small or irregular for a successful separation. An approach is presented that utilizes the good detectability of tidal magnetic signals to detect changes in the oceanic electric conductivity distribution. Ocean circulation, tides, and the resultant magnetic fields are calculated with a global general ocean circulation model coupled to a 3-D electromagnetic induction model. For the decay of the meridional overturning circulation, as an example, the impact of climate variability on tidal oceanic magnetic signals is demonstrated. Total overturning decay results in anomalies of up to 0.7 nT in the radial magnetic M2 signal at sea level. The anomalies are spatially heterogeneous and reach in extended areas 30% or more of the unperturbed tidal magnetic signal. The anomalies should be detectable in long time series from magnetometers on land or at the ocean bottom. The anomalies at satellite height (430 km) reach 0.1 nT and pose a challenge for the precision of the Swarm mission. Climate variability induced deviations in the tide system (e.g., tidal velocities and phases) are negligible. Changes in tidal magnetic fields are dominated by changes in seawater salinity and temperature. Therefore, it is concluded that observations of tidal magnetic signals could be used as a tool to detect respective state changes in the ocean.

1. Introduction

The Swarm satellite magnetometer mission (launched November 2013) proposes to measure Earth's magnetic field with unprecedented precision [*Friis-Christensen et al*., 2006]. In addition, Swarm extends previous satellite-based magnetometer time series (e.g., from Ørsted and CHAMP) which further improves the precision. This allows new possibilities for the observation of oceanic processes. The extraction of the M2 tidal signals in CHAMP satellite magnetometer data was first demonstrated by *Tyler et al*. [2003]. *Sabaka et al*. [2016] repeated the M2 extraction for Swarm data and could in addition demonstrate the detection of the N2 tide. In contrast to static or irregular oceanic signals, the tides' stable temporal frequency and spatial pattern allow their separation from other (often much larger) contributions to the Earth's observed magnetic field [see, e.g., *Sabaka et al*., 2015]. However, not only satellite magnetometers are usable for ocean observations. Tidal signals are also detected by terrestrial magnetometers at the ocean bottom [e.g., *Schnepf et al*., 2014] and on land [e.g., *Kuvshinov et al*., 2006]. Other time varying oceanic contributions to the magnetic field originating from, e.g., the general circulation, seasonal effects, ENSO, and tsunamis, are small [$\pm$0.2 nT, *Manoj et al*., 2006]. In addition, the temporal and spatial variations are irregular and the signal's uncertainty is of comparable size [*Irrgang et al*., 2016a]. Consequently, a respective detection is difficult and most promising in situ, for example, by ocean bottom magnetometers, moorings or cables [see, e.g., *Larsen*, 1991; *Fujii et al*., 1995; *Manoj et al*., 2010; *Rayner et al*., 2011].

In this study, a new approach is presented that uses the good separability of tidal signals to overcome the limited observability of magnetic signals which are related to changes in the ocean's general circulation. The approach is presented for the example of climate change induced deviations in the oceanic overturning circulation. These changes are very slow and the relevant ocean velocities are very small. Consequently, a direct observation by satellite magnetic measurements would be challenging.

Irrgang et al. [2016b] demonstrated the importance of realistic 3-D ocean electric conductivity (σ) distributions to model magnetic signals originating in the general circulation. In general, the authors suggested to

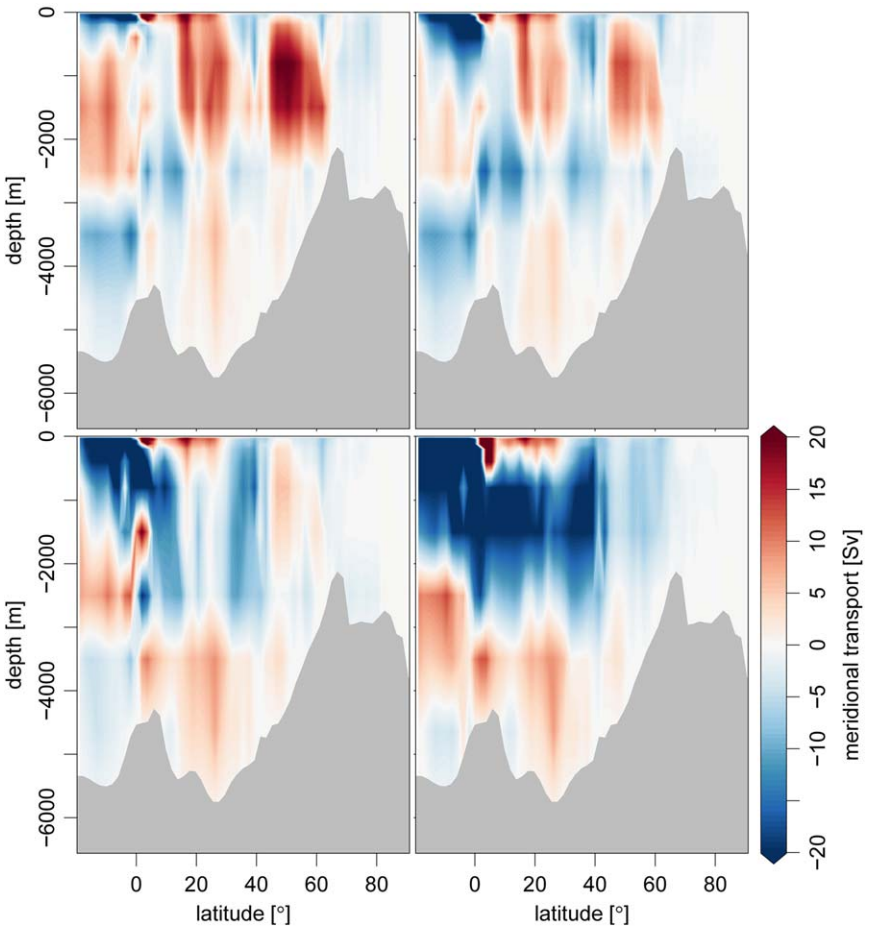

Figure 1. Stages of AMOC decay. Annual mean values. (top) REFAMOC and AMOC70. (bottom) AMOC30 and NOAMOC.

use a realistic conductivity distribution in studies that include ocean induction processes. Here their findings are applied to magnetic fields generated by ocean tides. The authors stated that seasonal variations of salinity (S) and temperature (T) do not lead to significant changes in σ and therefore in the magnetic field. However, nonseasonal processes exist that do change the oceanic S and T distributions significantly. Most of these changes are forced by climate variations [e.g., *Intergovernmental Panel on Climate Change* (*IPCC*), 2013].

To study the question if climate variability induced changes are in principle observable in magnetic field measurements of the ocean, the breakdown of the Atlantic meridional overturning circulation (AMOC) is simulated by a global general ocean circulation model. Note, that this is only an example for possible changes in the ocean that are induced by climate variability [e.g., *Gleckler et al*., 2016]. The possibility of a weakening or breakdown of the AMOC is usually attributed to increased freshwater flux into high latitude oceans which results from the melting of Greenland glaciers [*Rahmstorf*, 1995; *Yu et al*., 2016]. Other recently discussed influences to the state of the overturning include (among others): increased runoff from Alaska and Canada [*Harig and Simons*, 2016], arctic deep water formation [*Yang et al*., 2016b], melting at Antarctica [*Patara and Böning*, 2014], wind forcing [*Stewart and Thompson*, 2012; *Yang et al*., 2016a], and breaking of internal waves [*Mashayek et al*., 2015]. This paper is not about to add to the ongoing discussion and uses only one of the possible mechanisms to generate deviations in the AMOC: glacial melting on Greenland. The question to what extent Greenland melting is influencing the AMOC is under much debate, too [*Yu et al*., 2016]. Respective results from numerical ocean models strongly depend on the model's resolution [*Matthijs et al*., 2014], the incorporated mixing schemes [*Mashayek et al*., 2015], and the coupling to atmosphere models [*Stouffer et al*., 2006; *Saenko et al*., 2007]. Strength, spatial extent, and location of the freshwater input play a crucial role, too [*Roche et al*., 2010; *Yu et al*., 2016].

Furthermore, observed rates of Greenland mass loss show high variability [*Harig and Simons*, 2016]. For example, the observations range from 29 Gt/a during 2013–2014 to 562 Gt/a during 2012–2013 [*Velicogna and Wahr*, 2013; *Tedesco et al*., 2015]. Consequently, reliable projections into the future are difficult.

Discussing and debating the mechanisms of climate change in the oceanic overturning circulation system is beyond the scope of this paper. Instead, we aim to use the published results to generate ocean state examples which are within the range of expected climate variability induced changes. The generation of the oceanic example states and the experiment design is explained in section 2. The used global general ocean circulation model and the generation of tidal electric currents is described in section 3. The electromagnetic induction model is described in section 4. The results of the experiment are presented, compared and discussed in section 5. The paper closes with conclusions and a summary in section 6.

2. Experiment Design

Different states of AMOC decay are modeled and compared by the tidal magnetic field they would emit. In the used ocean model (see section 3), the AMOC decay is triggered by additional freshwater input into the North Atlantic. The governing mechanisms and the sensitivity of the AMOC are still under much debate (see section 1). The AMOC sensitivity to freshwater input depends on the used model, the model's resolution and the applied mixing schemes [*Yu et al*., 2016]. In addition, the model's sensitivity depends on the location and spatial extent of meltwater input and the inclusion of atmospheric feedbacks by the use of coupled atmosphere/ocean models [*Saenko et al*., 2007]. Therefore, we separate results and discussion from a possible misleading time reference and define four representative stages of AMOC decay. Nonetheless, the amount and impact of the applied freshwater input is in correspondence with the literature, i.e., 0.1–1.0 Sv of additional freshwater lead to substantial weakening or shut down within 50–100 years [e.g., *Stouffer et al*., 2006]. The defined stages are plotted in Figure 1 and represent annual mean values: REFAMOC (undisturbed reference AMOC), AMOC70 (small decay), AMOC30 (serious decay), and NOAMOC (total shutdown).

The REFAMOC shows an upper overturning cell where water is transported to the north in the upper layers (0–1000 m). The water sinks at 60°N down to depths of 1500–3000 m and is transported to the south. The maximum of the upper cell is 22 Sv and is located at 50° north and at 1000 m depth. The upper cell is stronger [the observed value is 18.7 Sv, *Rayner et al*., 2011] and not as continuous as assumed [e.g., *Yu et al*., 2016]. A weak counter-clockwise transport exists in the deep ocean (3000–4000 m). Values and pattern of REFAMOC are well within the range for commonly used ocean models [*Griffies et al*., 2009]. The acronyms AMOC70 and AMOC30 refer to the percentage of weakening in REFAMOC's upper overturning cell maximum, i.e., the AMOC70 and AMOC30 stages show northward transports of 15 Sv and 6 Sv, respectively. The AMOC70 pattern is similar to REFAMOC but shows smaller northward transport. The AMOC30 pattern must already be considered as serious AMOC decay. Most of the upper overturning cell is interrupted and reversed. Only a very small cell of the former upper overturning branch remains around the reference maximum. The NOAMOC represents a stage where the entire upper branch is reversed.

3. Ocean Model

Ocean velocities and seawater properties of the Greenland hosing experiment are simulated with the Ocean Model for Circulations and Tides (OMCT) [*Dobslaw and Thomas*, 2007]. The baroclinic model uses nonlinear momentum equations and calculates temporal variable distributions of T, S, velocity ($\vec{v}$) and sea surface height (SSH). In addition to the atmospheric forcing (details below), an ephemerides based full tidal potential is used to force the ocean.

Tide induced changes from all tides and the ocean's general circulation are simulated together and interact nonlinearly [*Thomas et al*., 2001]. Mass is conserved by following *Greatbatch* [1994]. Consequently, boundary freshwater flux will change the modeled ocean mass and the modeled sea level. The grid spacing is 1.875° ×1.875° in 13 layers and the time step is 30 min. The atmospheric forcing consists of 6 hourly fields for wind stress, freshwater flux, and heat flux from the ERA-Interim reanalysis of the European

Centre for Medium-Range Weather Forecasts (ECMWF) [*Uppala et al*., 2008]. The OMCT in this configuration produces a realistic magnetic signal of the ocean's general circulation [*Irrgang et al*., 2016b,2016a]. Due to model resolution small-scale features like eddies are not resolved and the respective magnetic signals are underestimated [*Manoj et al*., 2006]. However, the focus of this study is climate change induced basin wide deviations in salinity and temperature distribution. These deviations are supposed to be well resolved.

From the modeled S, T, and pressure (P), the seawater electric conductivity is calculated by using the oce package [*Kelley and Richards*, 2015] which uses the Gibbs-SeaWater equation [TEOS-10, *IOC et al*., 2010].

M2 electric currents are calculated in three steps from the 3-D distributions of conductivity and velocity. First, the ocean currents are multiplied with the local conductivity and subsequently integrated from the ocean bottom to the sea surface:

$$\vec{V}(\phi,\theta,t)=\int_{-H}^{SSH}\sigma(\phi,\theta,z,t)\vec{v}(\phi,\theta,z,t)dz. \tag{1}$$

Second, M2 amplitude and phase are separated from $\vec{V}$ by using the tidem routine of the oce package. The result is $\vec{V}_{M2}$. To ensure reasonable separation, 1 year of model data with hourly resolution is used. In contrast to an ocean model which is forced by the M2 potential only, the results of the presented approach also contain signals that are not or not directly of M2 tidal origin but share the same very narrow frequency band. In this way, the presented approach is more similar to the tidal separation method used in observations.

Third, M2 electric currents are calculated by the cross-product of $\vec{V}_{M2}$ and the Earth's ambient magnetic field ($\vec{B}$), which is derived from GRIMM-3 [*Lesur et al*., 2008, up to degree and order 18]:

$$\vec{j}_{M2}(\phi,\theta)=\vec{V}_{M2}(\phi,\theta)\times\vec{B}(\phi,\theta). \tag{2}$$

Our study covers changes that are supposed to happen within 10–100 years [*Stouffer et al*., 2006]. In our study, secular changes in Earth's ambient magnetic field are neglected and $\vec{B}$ is assumed constant in equation (2). Note, that when comparing our model results with observations the effect of (well observed) changes in $\vec{B}$ should be removed in the latter.

4. Electromagnetic Induction Model

To calculate the M2 magnetic field, the tidal electric current $\vec{j}_{M2}$ (equation (2)) is used as input for the 3-D electromagnetic induction model of *Kuvshinov* [2008]. This volume integral equation model solves Maxwell's equations in frequency space. The model's horizontal resolution is $1^\circ \times 1^\circ$. In the vertical, a 1-D spherically symmetric mantle conductivity following *Püthe et al*. [2015] is used below a thin spherical layer of variable electric conductance at the Earth's surface. We differ from the approach described in *Kuvshinov* [2008] only in the calculation of this surface layer's electric conductance. To derive the conductance of the induction model's thin surface layer, *Kuvshinov* [2008] combine the sediment conductance (using the method of *Everett et al*. [2003] with data from *Laske and Masters* [1997]) with an ocean conductance based on climatological S, T, and P. In our study, the oceanic component of the shell conductance is calculated from OMCT's modeled σ values (section 3) and represents annual mean values which correspond to the respective AMOC stages (see section 2), i.e., the M2 signals of the four AMOC stages are calculated with corresponding different shell conductances. This step influences both the calculated tidal magnetic fields and the resulting differences between the AMOC stages significantly. If the shell conductance is not adjusted and different σ distributions are only used in the calculation of the currents $\vec{j}_{M2}$ (i.e., the sources for the induction process), the differences in the resulting tidal magnetic fields (section 5) are overestimated by up to 20%.

In addition, the tidal magnetic field depends on the resistivity distribution in the lithosphere and the upper mantle [*Schnepf et al*., 2014, 2015]. However, our study focuses on differences between tidal magnetic fields across several decades and so the lithospheric and upper mantle resistivity distribution is considered constant.

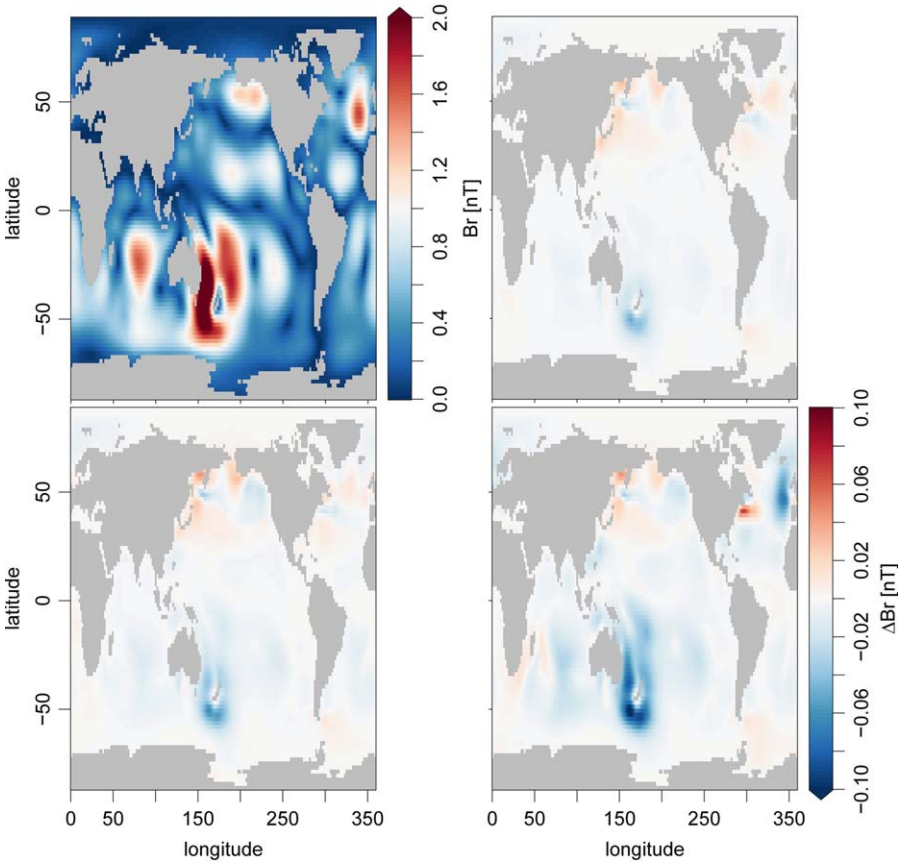

Figure 2. M2 amplitude of radial magnetic field at satellite altitude (430 km above sea level). (top left) M2 amplitude of REFAMOC. (top right) M2 amplitude difference, AMOC70 minus REFAMOC. (bottom left) AMOC30 minus REFAMOC. (bottom right) NOAMOC minus REFAMOC.

5. Results

As described in sections 3 and 4, the amplitude of the radial magnetic field component of the M2 tide from REFAMOC is calculated at Swarm altitude (430 km above sea level) and plotted in Figure 2 (top left plot). A large ring-like anomaly of up to 3.1 nT encircles New Zealand. Additional pronounced maxima exist in the North Pacific, the North Atlantic, and in the Indian Ocean. The pattern of the M2 magnetic signal is within the range of the literature and the amplitudes are comparable with results from other forward models [e.g., *Schnepf et al.*, 2015, Figure 1, *Sabaka et al.*, 2015, Figure 12]. Nonetheless, some discrepancies are evident. For example, the amplitudes in the Indian Ocean and the North Atlantic are smaller than in the literature. Especially in relation to the high signal strength around New Zealand. Since the calculations in the literature are based on barotropic velocities derived from satellite altimetry observations and our calculations are based on modeled baroclinic velocities, discrepancies are expected. Our study uses a 3-D conductivity distribution generated from an ocean model rather than climatology values or the commonly used global mean σ in the literature. We consistently use the same conductivity distribution to generate the M2 electric currents (section 3) and to calculate the induction model's shell conductance (section 4). Finally, the M2 tide is simulated together with other tides and the general ocean circulation (see section 3). With this background, discrepancies between model-based studies seem reasonable. However, when Figure 2 is compared to observations of M2 magnetic signal amplitudes from Swarm and CHAMP [*Sabaka et al.*, 2016], the signal strength in the Indian Ocean and the North Atlantic is too weak. The reason for this discrepancy remains to be investigated.

The additional plots of Figure 2 show the impact of the simulated climate variability (see section 2) on the M2 radial magnetic signal's amplitude. Depicted are the differences of AMOC70, AMOC30, and

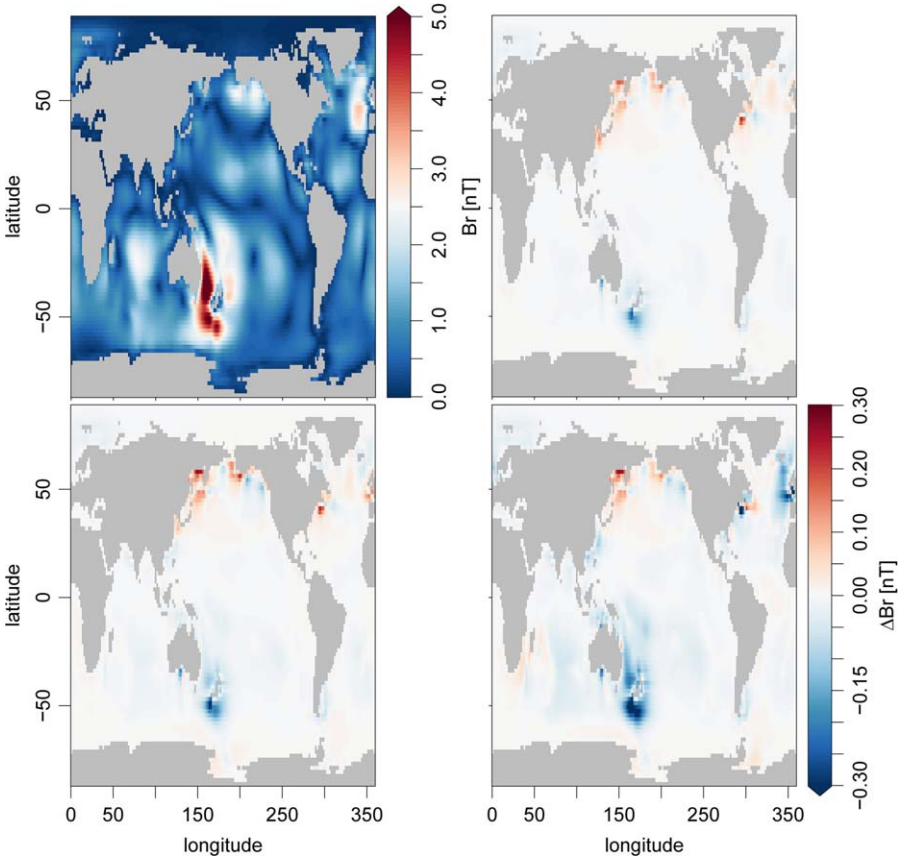

Figure 3. M2 amplitude of radial magnetic field at sea level. (top left) M2 amplitude of REFAMOC. (top right) M2 amplitude difference, AMOC70 minus REFAMOC. (bottom left) AMOC30 minus REFAMOC. (bottom right) NOAMOC minus REFAMOC.

NOAMOC with respect to REFAMOC. Despite that additional freshwater is added to the North Atlantic only, deviations in the M2 magnetic signal occur globally. The deviations are nonuniform and negative in most areas. For example, the southern and central parts of the Pacific, the Atlantic, and the whole Indic ocean show a weakening of the magnetic signal compared to REFAMOC. The largest decreases occur around New Zealand but are not exactly colocated with the maximum of the M2 signal itself (see top left plot). The maximal decrease ranges from −0.05 nT in AMOC70 to −0.1 nT in NOAMOC. Positive deviations occur around the Drake Passage and in the northern part of the Pacific and Atlantic. Given this study's underestimation of the M2 signal in the Indian ocean, the differences in this region may be underestimated, too.

Apart from satellites, ocean electromagnetic field observations are also possible by floats, cruises, deep sea cables [*Fujii et al*., 1995; *Szuts*, 2012], land-based magnetometers [*Kuvshinov et al*., 2006; *Kuvshinov and Utada*, 2010], and ocean bottom magnetometers [*Luther et al*., 1991; *Schnepf et al*., 2014]. Therefore, Figure 3 shows the same quantities as Figure 2 at sea level. Naturally, the magnetic signal at sea level is stronger and less smooth than the signal at satellite altitude. The M2 magnetic amplitude reaches 6.6 nT and the deviations range from −0.3 nT in AMOC70 to −0.7 nT in NOAMOC. Note that the axial magnetic fields modeled by the used induction model (section 4) are approximately the same for sea level and ocean bottom.

Independent of the observation altitude, the difference pattern of AMOC70 and AMOC30 is very similar and differs only in strength. The difference pattern of NOAMOC shows an additional dipole signal in the North Atlantic which is a result of the final vanishing of the upper overturning cell (see Figure 1, bottom right). Since apart from this dipole the plotted difference fields are similar (except for a scaling factor), plots for AMOC70 and AMOC30 are not included from now on.

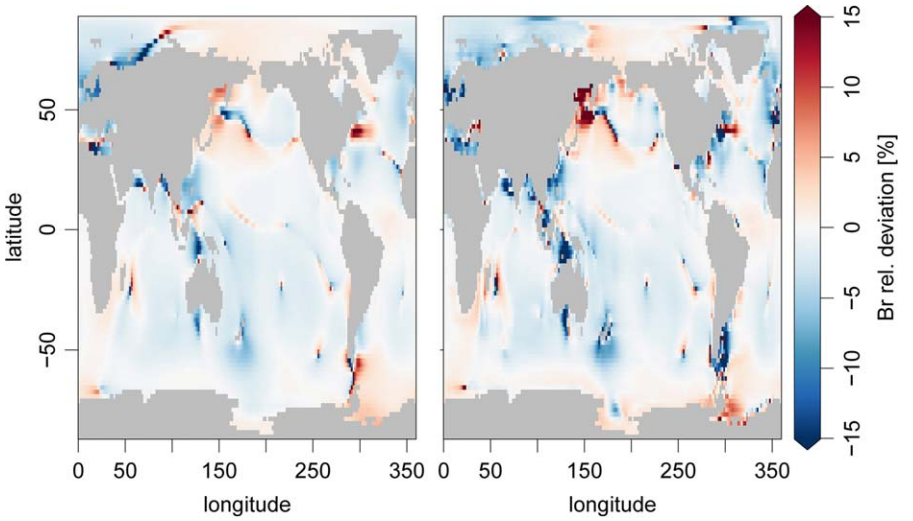

Figure 4. Relative deviation (equation (3)) of radial magnetic field M2 amplitude of NOAMOC. (left) At satellite altitude (430 km above sea level). (right) At sea level.

To show the differences of Figures 2 and 3 in relation to the total signal strength, relative deviations (*RD*) of an AMOC stage (e.g., NOAMOC) are defined in relation to REFAMOC as:

$$RD(f) = 100 \times \frac{f(NOAMOC) - f(REFAMOC)}{|f(REFAMOC)|}, \tag{3}$$

where f is an arbitrary operator, e.g., the magnetic field or the salinity operator.

Figure 4 shows the differences of Figures 2 and 3 as relative deviations in relation to REFAMOC. The relative deviations in the radial M2 magnetic signal are around or below 5% for most parts of the world oceans. Higher deviations of 30% or more are most pronounced at sea level (right plot) and occur in many coastal regions, e.g., around Patagonia, the Weddell Sea, the Indonesian Troughflow, and north of Japan. In addition, high very localized relative deviations occur around amphidromic points and originate in small shifts in the tidal system during the simulation.

To quantify how the deviations in the magnetic field are generated, the conductivity weighted and depth integrated velocity ($\vec{V}_{M2}$, equations (1) and (2)) is plotted in Figure 5. $\vec{V}_{M2}$ provides the source for the electric currents $\vec{j}_{M2}$ (equation (2)) which in turn provide the sources for the induction process. Because in $\vec{V}_{M2}$ the cross-product with Earth's ambient magnetic field is not yet incorporated, $\vec{V}_{M2}$ allows a clearer view of the

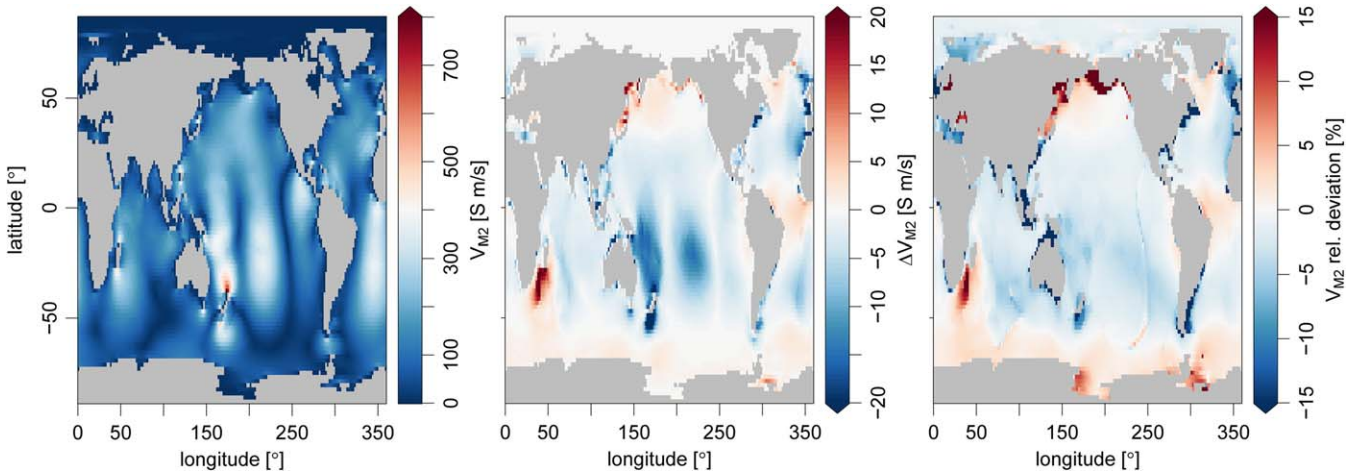

Figure 5. M2 amplitude of conductivity weighted and depth integrated zonal velocity ($\vec{V}_{M2}$, equation (1)). (left) M2 amplitude of REFAMOC. (middle) Amplitude difference, NOAMOC minus REFAMOC. (right) Relative deviation (equation (3)) of NOAMOC.

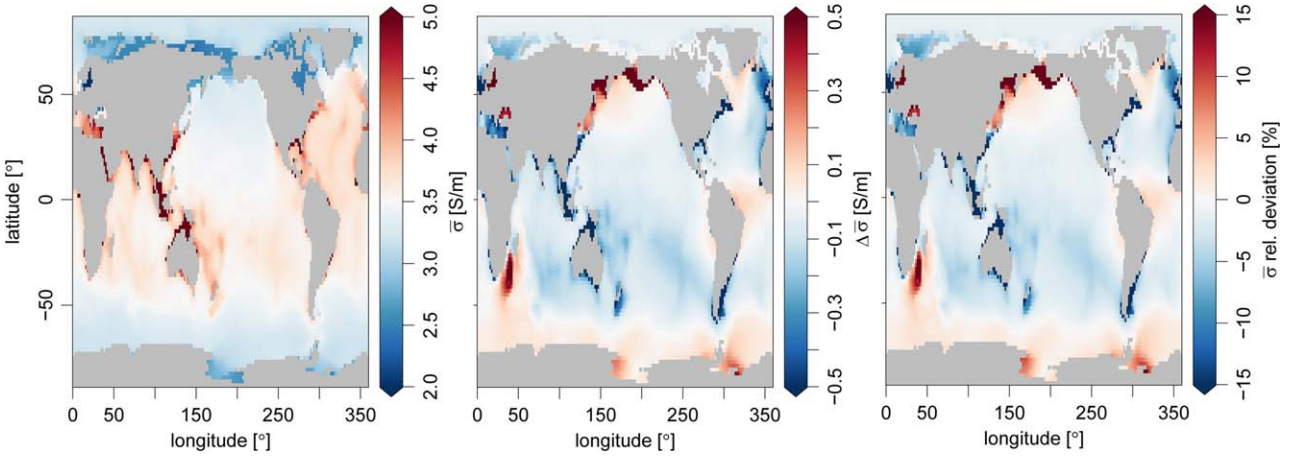

Figure 6. Vertical mean conductivity. (left) Conductivity of REFAMOC. (middle) Conductivity difference, NOAMOC minus REFAMOC. (right) Relative deviation (equation (3)) of NOAMOC.

oceanic contributions to the magnetic field than $\vec{j}_{M2}$. $\vec{V}_{M2}$ is a vector and the following plots depict only the zonal component of $\vec{V}_{M2}$. Nonetheless, the results apply for the remaining components, too. The right plot of Figure 5 shows the typical M2 tidal amplitude pattern of ocean zonal velocity which is imprinted in $\vec{V}$ by the multiplication with $\vec{v}$ in equation (1). Broad maxima of 350 Sm/s occur in the Pacific and the Atlantic. The global maximum is located north of New Zealand and reaches 800 Sm/s. In the middle plot, deviations of $\vec{V}_{M2}$ between REFAMOC and NOAMOC are shown and amount to $\pm$20 Sm/s in large areas (local maxima range from $-$74 to 38 Sm/s). The M2 tidal zonal velocity pattern is still visible but vanishes in the relative deviations (right plot). Naturally, the similarities between the pattern of $\vec{V}_{M2}$ changes and ocean magnetic field changes are strong (see Figure 4 but note that Figure 4 is based on all $\vec{V}_{M2}$ vector components). Likewise, the relative differences of $\vec{V}_{M2}$ and the tidal magnetic field have a comparable range ($\pm$30%).

In the presented experiment (section 2), the climate induced changes in Figures 2–5 can be generated either by changes in the ocean velocity fields, changes in the ocean conductivity field or by sea level changes (see equation (1)). Figure 6 shows the vertical mean of the ocean conductivity. In the left plot the conductivity itself is plotted and shows a strong latitudinal dependence, i.e., low conductivity at the poles (cool and fresh water) and high conductivity in the tropics (warm and salty water) [*Irrgang et al.*, 2016b]. The influence of the ocean's bathymetry is visible (e.g., mid ocean ridges, continental shelfs, depth differences between Atlantic and Pacific). Most of the climate change induced deviations in the depth averaged conductivity (middle plot) are below 0.5 S/m but can locally (e.g., in shallow areas) amount to $\pm$2 S/m.

The relative deviations of the depth averaged ocean conductivity and $\vec{V}_{M2}$ are highly correlated. The differences between the right plots of Figures 5 and 6 are small and can be explained by deviations in the respective tidal amphidromic system which are mainly induced by sea level rise (not plotted). Changes in the M2 amplitude of SSH and ocean velocity between REFAMOC and NOAMOC are below 2% (not plotted). These changes amount to small shifts in the location of the amphidromic points which can be seen in Figure 4 as small dipole dots, e.g., in the Pacific. Furthermore, small shifts of up to $\pm 2^\circ$ in the phase of the M2 ocean velocities occur (not plotted). These phase shifts do not significantly influence the induced magnetic signal but can be seen as thin lines in Figure 5 (right plot) at locations where the M2 pattern (Figure 5, left plot) is zero and even small shifts result in higher relative deviations.

Consequently, the climate variability induced deviations in $\vec{V}$ (and therefore in the induced magnetic fields) are mostly explained by changes in σ. Climate variability induced changes in σ can in turn result from S, T or P changes (or combinations). Respective changes in P are very small and the resulting σ changes are negligible (not plotted). Figure 7 compares the zonal mean relative deviations of σ, S and T. The additional freshwater input leads to surface cooling (bottom left plot) and freshening (bottom right plot), as well as subsequent weakening of the AMOC [see *Yu et al.*, 2016]. The resultant changes in the meridional heat and salt transport allow the high latitude mixing between the upper and deep ocean to occur in lower latitudes, too (see Figure 1). The result is salinification and warming of deeper ocean layers (in addition to the opposite effect in the upper ocean). The meridional σ deviations (top right plot) are dominated by changes in T

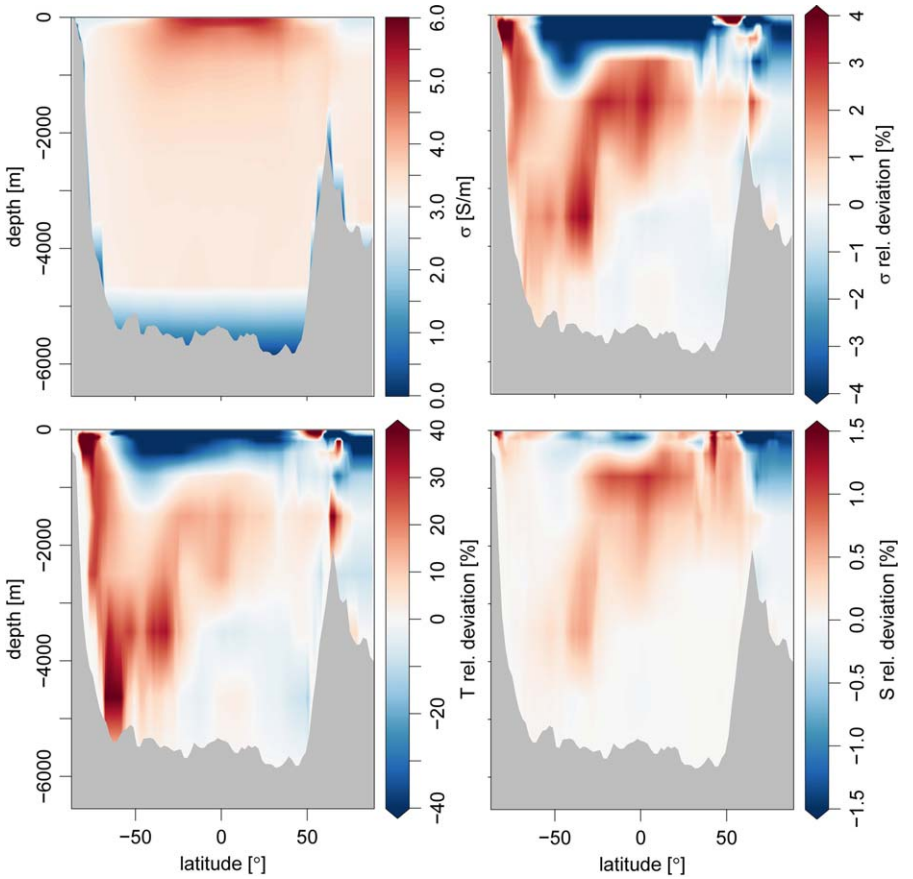

Figure 7. Global zonal mean conductivity, temperature, and salinity. (top left) Conductivity of REFAMOC. (top right) Relative conductivity deviation of NOAMOC. (bottom left) Relative temperature deviation of NOAMOC. (bottom right) Relative salinity deviation of NOAMOC.

(bottom left plot) which are slightly modulated by changes in S (bottom right plot). In the horizontal integral sense of equation (1) (see Figure 6), the S and T changes in the upper 1000 m of the ocean dominate over the changes in the deep ocean. These S and T changes result in the plotted deviations of $\vec{V}_{M2}$ (Figure 5) and of the radial magnetic M2 fields (Figures 2–4) and explain the globally mostly negative anomalies and the positive anomalies in the polar regions. Note, that the σ-differences plotted in Figures 6 and 7 are independent of any particular tide. Whether σ-deviations on specific geographical locations influence the tidal magnetic field (or not) depends on the analyzed tide itself. Other tidal pattern than the M2, e.g., S2, N2, and especially K1, O1 [*Kuvshinov et al*., 2006; *Sabaka et al*., 2016], will highlight σ-deviations in different geographic regions.

6. Summary and Conclusions

A global general ocean model was forced with additional freshwater input in the arctic North Atlantic region to generate different stages of AMOC decay. From these stages the radial magnetic signal of the M2 ocean tide was calculated and compared. A correlation between changes in the M2 magnetic signal and stages of AMOC decay is demonstrated. In most areas, AMOC decay results in a decreased magnetic M2 signal. Local positive anomalies occur, e.g., in the Antarctic circumpolar current region or around Alaska. The deviations in the M2 magnetic signal between a reference AMOC and full AMOC decay amount to 0.1 nT (0.7 nT) at satellite height (sea level) and are results of changes in conductivity, i.e., changes in salinity and temperature. Other contributions to the M2 magnetic signal, i.e., changes in sea level, M2 phases and M2 velocities are negligible. Given the good separability of M2 ocean tides in magnetic observations, tidal magnetic observations could be used as a reliable tool to detect changes in the state of the oceans. Since the amount of climate change induced freshwater input and its impact in the ocean is still under debate and results are highly model dependent, the values and pattern of this paper should be evaluated as a

demonstration in principle of the sensitivity of tidal magnetic signals with respect to climate variability. For more realistic results, the analysis will be repeated with coupled simulations of atmosphere and ocean [*Stouffer et al*., 2006; *Yang et al*., 2016a]. These simulations should include other important effects such as global warming, i.e., greenhouse gasses [*Gleckler et al*., 2016] or the El Niño Southern Oscillation. Furthermore, the analysis will be extended to other tidal frequencies (e.g., O1) to resolve conductivity changes in other geographical locations of the ocean, such as the high latitudes. In our simulations, the M2 magnetic field deviations reach the reported values after 50–100 years. On shorter time spans the values amount to a fraction of the reported values. Therefore, preferably long observation time series of tidal magnetic signals, e.g., from CHAMP+Swarm should be analyzed for temporal changes (see M2 signals from Swarm and CHAMP in *Sabaka et al*. [2016]). The AMOC decay impact on M2 signals is 0.1 nT at satellite altitude. This matches in principle the nominal Swarm precision [*Friis-Christensen et al*., 2006; *Olsen et al*., 2007]. However, the detection of the presented signals in satellite-based magnetometer measurements may be challenging today. Nonetheless, the precision of the observations might improve with longer observation time series, by future processing improvements or through future magnetometer satellite missions. In addition, terrestrial magnetometers should be used. The expected changes at sea level (or ocean bottom) are of the order of several 0.1 nT and should be detectable by magnetometers on land, at ocean bottom, by deep sea telecommunication cables or in induction based Tsunami early warning networks [*Kuvshinov et al*., 2006; *Kuvshinov and Utada*, 2010; *Schnepf et al*., 2014; *Rabinovich and Eble*, 2015]. Therefore, future similar sensitivity studies should also consider deviations in the nonradial magnetic fields and in the electric fields as well.

Acknowledgments

This study has been funded by the Helmholtz Foundation and the German Research Foundation (SPP1788 Dynamic Earth). The authors thank for the opportunity to use ERA-Interim data from the European Centre for Medium-Range Weather Forecasts and facilities from the German High Performance Computing Centre for Climate and Earth System Research. Researchers interested in using data from the OMCT may contact Maik Thomas (maik.thomas@gfz-potsdam.de). Researchers interested in the 3-D electromagnetic induction model may contact Alexey Kuvshinov (kuvshinov@erdw.ethz.ch). Furthermore, we very much like to thank Alexander Grayver and the two reviewers for their support as well as their very useful comments and corrections.

References

Dobslaw, H., and M. Thomas (2007), Simulation and observation of global ocean mass anomalies, *J. Geophys. Res. Oceans*, *112*, C05040, doi:10.1029/2006JC004035.

Everett, M. E., S. Constable, and C. G. Constable (2003), Effects of near-surface conductance on global satellite induction responses, *Geophys. J. Int.*, *153*(1), 277–286.

Friis-Christensen, E., H. Lühr, and G. Hulot (2006), Swarm: A constellation to study the earth's magnetic field, *Earth Planets Space*, *58*(4), 351–358.

Fujii, I., L. J. Lanzerotti, H. Utada, H. Kinoshita, J. Kasahara, L. V. Medford, and C. G. Maclennan (1995), Geoelectric power spectra over oceanic distances, *Geophys. Res. Lett.*, *22*(4), 421–424.

Gleckler, P. J., P. J. Durack, R. J. Stouffer, G. C. Johnson, and C. E. Forest (2016), Industrial-era global ocean heat uptake doubles in recent decades, *Nat. Clim. Change*, *6*, 394–398.

Greatbatch, R. J. (1994), A note on the representation of steric sea-level in models that conserve volume rather than mass, *J. Geophys. Res.*, *99*(C6), 12,767–12,771.

Griffies, S. M., A. Biastoch, C. Boening, F. Bryan, G. Danabasoglu, E. P. Chassignet, M. H. England, R. Gerdes, H. Haak, R. W. Hallberg, et al. (2009), Coordinated Ocean-ice Reference Experiments (COREs), *Ocean Modell.*, *26*(1–2), 1–46.

Harig, C., and F. J. Simons (2016), Ice mass loss in Greenland, the gulf of Alaska, and the Canadian archipelago: Seasonal cycles and decadal trends, *Geophys. Res. Lett.*, *43*, 3150–3159, doi:10.1002/2016GL067759.

IOC, SCOR, and APSO (2010), The international thermodynamic equation of seawater—2010: Calculation and use of thermodynamic properties, Intergovernmental Oceanographic Commission, *Manuals and Guides 56*, UNESCO, Paris.

Intergovernmental Panel on Climate Change (IPCC) (2013), *Climate Change 2013: The Physical Science Basis. Contribution of Working Group I to the Fifth Assessment Report of the Intergovernmental Panel on Climate Change*, 1535 pp., Cambridge Univ. Press, Cambridge, U. K.

Irrgang, C., J. Saynisch, and M. Thomas (2016a), Ensemble simulations of the magnetic field induced by global ocean circulation: Estimating the uncertainty, *J. Geophys. Res*, *121*, 1866–1880, doi:10.1002/2016JC011633.

Irrgang, C., J. Saynisch, and M. Thomas (2016b), Impact of variable seawater conductivity on motional induction simulated with an ocean general circulation model, *Ocean Sci.*, *12*(1), 129–136.

Kelley, D., and C. Richards (2015), *oce: Analysis of Oceanographic Data*, R package version 0.9-17, Dan Kelley, Halifax, Canada.

Kuvshinov, A., and H. Utada (2010), Anomaly of the geomagnetic Sq variation in Japan: Effect from 3-D subterranean structure or the ocean effect?, *Geophys. J. Int.*, *183*(3), 1239–1247.

Kuvshinov, A., A. Junge, and H. Utada (2006), 3-D modelling the electric field due to ocean tidal flow and comparison with observations, *Geophys. Res. Lett.*, *33*, L06314, doi:10.1029/2005GL025043.

Kuvshinov, A. V. (2008), 3-D global induction in the oceans and solid earth: Recent progress in modeling magnetic and electric fields from sources of magnetospheric, ionospheric and oceanic origin, *Surv. Geophys.*, *29*(2), 139–186.

Larsen, J. (1991), Transport measurements from in-service undersea telephone cables, *IEEE J. Oceanic Eng.*, *16*(4), 313–318.

Laske, G., and G. Masters (1997), A global digital map of sediment thickness, *Eos Trans. AGU*, *78*(46), Fall Meet. Suppl., F483.

Lesur, V., I. Wardinski, M. Rother, and M. Mandea (2008), GRIMM: The GFZ reference internal magnetic model based on vector satellite and observatory data, *Geophys. J. Int.*, *173*(2), 382–394.

Luther, D. S., J. H. Filloux, and A. D. Chave (1991), Low-frequency, motionally induced electromagnetic-fields in the ocean. 2: Electric-field and eulerian current comparison, *J. Geophys. Res.*, *96*(C7), 12,797–12,814.

Manoj, C., A. Kuvshinov, S. Maus, and H. Lühr (2006), Ocean circulation generated magnetic signals, *Earth Planets Space*, *58*(4), 429–437.

Manoj, C., A. Kuvshinov, S. Neetu, and T. Harinarayana (2010), Can undersea voltage measurements detect tsunamis?, *Earth Planets Space*, *62*(3), 353–358.

Mashayek, A., R. Ferrari, M. Nikurashin, and W. R. Peltier (2015), Influence of enhanced abyssal diapycnal mixing on stratification and the ocean overturning circulation, *J. Phys. Oceanogr.*, *45*(10), 2580–2597.

Matthijs, d. T., H. A. Dijkstra, W. Weijer, M. W. Hecht, M. E. Maltrud, and E. van Sebille (2014), Response of a strongly eddying global ocean to North Atlantic freshwater perturbations, *J. Phys. Oceanogr.*, *44*(2), 464–481.

Olsen, N., T. J. Sabaka, and L. R. Gaya-Pique (2007), Study of an improved comprehensive magnetic field inversion analysis for Swarm—Final report number 1, *Tech. Rep. 1*, Danisch Natl. Sci. Cent., Lyngby, Denmark.

Patara, L., and C. W. Böning (2014), Abyssal ocean warming around Antarctica strengthens the Atlantic overturning circulation, *Geophys. Res. Lett.*, *41*, 3972–3978, doi:10.1002/2014GL059923.

Püthe, C., A. Kuvshinov, A. Khan, and N. Olsen (2015), A new model of earth's radial conductivity structure derived from over 10 yr of satellite and observatory magnetic data, *Geophys. J. Int.*, *203*(3), 1864–1872.

Rabinovich, A. B., and M. C. Eble (2015), Deep-ocean measurements of tsunami waves, *Pure Appl. Geophys.*, *172*(12, SI), 3281–3312.

Rahmstorf, S. (1995), Bifurcations of the Atlantic Thermohaline Circulation in response to changes in the hydrological cycle, *Nature*, *378*(6553), 145–149.

Rayner, D., et al. (2011), Monitoring the Atlantic meridional overturning circulation, *Deep Sea Res., Part II*, *58*(17–18), 1744–1753.

Roche, D. M., A. P. Wiersma, and H. Renssen (2010), A systematic study of the impact of freshwater pulses with respect to different geographical locations, *Clim. Dyn.*, *34*(7–8), 997–1013.

Sabaka, T. J., N. Olsen, R. H. Tyler, and A. Kuvshinov (2015), CM5, a pre-Swarm comprehensive geomagnetic field model derived from over 12 yr of CHAMP, Orsted, SAC-C and observatory data, *Geophys. J. Int.*, *200*(3), 1596–1626.

Sabaka, T. J., R. H. Tyler, and N. Olsen (2016), Extracting ocean-generated tidal magnetic signals from swarm data through satellite gradiometry, *Geophys. Res. Lett.*, *43*, 3237–3245, doi:10.1002/2016GL068180.

Saenko, O. A., A. J. Weaver, D. Y. Robitaille, and G. M. Flato (2007), Warming of the subpolar Atlantic triggered by freshwater discharge at the continental boundary, *Geophys. Res. Lett.*, *34*, L15604, doi:10.1029/2007GL030674.

Schnepf, N. R., C. Manoj, A. Kuvshinov, H. Toh, and S. Maus (2014), Tidal signals in ocean-bottom magnetic measurements of the Northwestern Pacific: Observation versus prediction, *Geophys. J. Int.*, *198*(2), 1096–1110.

Schnepf, N. R., A. Kuvshinov, and T. Sabaka (2015), Can we probe the conductivity of the lithosphere and upper mantle using satellite tidal magnetic signals?, *Geophys. Res. Lett.*, *42*, 3233–3239, doi:10.1002/2015GL063540.

Stewart, A. L., and A. F. Thompson (2012), Sensitivity of the ocean's deep overturning circulation to easterly Antarctic winds, *Geophys. Res. Lett.*, *39*, L18604, doi:10.1029/2012GL053099.

Stouffer, R. J., et al. (2006), Investigating the causes of the response of the thermohaline circulation to past and future climate changes, *J. Clim.*, *19*(8), 1365–1387.

Szuts, Z. B. (2012), Using motionally-induced electric signals to indirectly measure ocean velocity: Instrumental and theoretical developments, *Prog. Oceanogr.*, *96*(1), 108–127.

Tedesco, M., et al. (2015), Arctic report card: Greenland ice sheet, *Tech. Rep. 1*, *Update for 2015*, NOAA, Wash.

Thomas, M., J. Sündermann, and E. Maier-Reimer (2001), Consideration of ocean tides in an OGCM and impacts on subseasonal to decadal polar motion excitation, *Geophys. Res. Lett.*, *28*(12), 2457–2460.

Tyler, R. H., S. Maus, and H. Luhr (2003), Satellite observations of magnetic fields due to ocean tidal flow, *Science*, *299*(5604), 239–241.

Uppala, S., D. Dee, S. Kobayashi, P. Berrisford, and A. Simmons (2008), Toward a climate data assimilation system: Status update of ERA interim, *Tech. Rep*. *115*, ECMWF Newsl, Reading, U. K.

Velicogna, I., and J. Wahr (2013), Time-variable gravity observations of ice sheet mass balance: Precision and limitations of the GRACE satellite data, *Geophys. Res. Lett.*, *40*, 3055–3063, doi:10.1002/grl.50527.

Yang, H., K. Wang, H. Dai, Y. Wang, and Q. Li (2016a), Wind effect on the Atlantic meridional overturning circulation via sea ice and vertical diffusion, *Clim. Dyn.*, *46*(11), 3387–3403.

Yang, Q., T. H. Dixon, P. G. Myers, J. Bonin, D. Chambers, and M. R. van den Broeke (2016b), Recent increases in Arctic freshwater flux affects Labrador Sea convection and Atlantic overturning circulation, *Nat. Commun.*, *7*, 10525, doi:10.1038/ncomms10525.

Yu, L., Y. Gao, and O. H. Ottera (2016), The sensitivity of the Atlantic meridional overturning circulation to enhanced freshwater discharge along the entire, eastern and western coast of Greenland, *Clim. Dyn.*, *46*(5–6), 1351–1369.